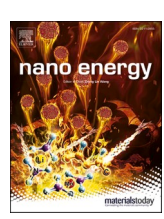
ELSEVIER

Contents lists available at ScienceDirect

Nano Energy

journal homepage: http://www.elsevier.com/locate/nanoen





The role of M@Ni₆ superstructure units in honeycomb-ordered layered oxides for Li/Na ion batteries

Zongxiang Hu, Mouyi Weng, Zhefeng Chen, Wenchang Tan, Shunning Li, Feng Pan

School of Advanced Materials, Peking University, Shenzhen Graduate School, Shenzhen 518055, People's Republic of China

ARTICLE INFO

Keywords: Li/Na ion batteries Honeycomb-ordered Electronic structure Superstructure unit

ABSTRACT

Honeycomb-ordered layered transition metal (TM) oxides, which are characteristic of a honeycomb network, have recently emerged as a novel class of cathode materials with high voltage and superior long-term cycling stability. Here, we provide a systematic first-principles study of the structural and electrochemical properties of honeycomb-ordered ANi_{2/3}M_{1/3}O₂ (A = Li and Na; M = As, Sb and Bi) aimed at disentangling the role of the M⁵⁺ species. Our results show that M endorses strong bonding with O and can give rise to superior thermodynamic stability of the compound as compared to ANiO₂ counterparts. Upon alkali deintercalation of ANi_{2/3}M_{1/3}O₂, there is a driving force for disproportionation of Ni³⁺ ions, which originates from the high-symmetric MO₆ octahedron and leads to the activation of both Ni²⁺/Ni³⁺ and Ni³⁺/Ni⁴⁺ redox couples. The distortion of NiO₆ octahedron can be modulated by the size of M, and a clear correlation is revealed between the distortion from octahedral symmetry and the electronic structures of the compounds, including the energy position of e_g orbitals and the temporary stabilization of Ni³⁺ ions. Both properties are linked to the voltage and polarization of the cathodes. This work provides a basis for further development of cathode materials based on honeycomb-ordered superstructure.

1. Introduction

Due to the rapid consumption of fossil fuels and the pressing demand for sustainable energy, it is crucial to develop cathode materials for lithium and sodium ion batteries with high energy capacity, long cycle life and low cost. Even with the rapid progress on multi-cation layered oxide $\text{LiNi}_x \text{Mn}_y \text{Co}_{1-x-y} \text{O}_2$, which is widely recognized as one of the most promising candidates for cathode, it is still challenging to achieve both high capacity and long cycle stability simultaneously [1,2]. In LiNi_xMn_yCo_{1-x-y}O₂, the transition metal (TM) elements are randomly distributed in the TM layer due to similar electronic structures between Ni, Mn and Co [3–12]. Apparently, its electrochemical performance is closely related to the single-cation layered oxides, which hints that multiple phase transformations in the form of layer gliding would be nearly unavoidable [13-15]. Layer gliding would result in abrupt crystal structural transition and diminished performance after long-term cycling [16-23]. Although chemical modulation via the optimization of the ratio between Ni, Mn and Co could alleviate this problem to some extent, other properties like capacity would be compromised [24-27]. Knowing that main group elements are more likely to contribute to structural stability, it is tempting to design new cathode materials by adding pentavalent main-group elements so as to tune the structure units and regulate the coordination environments that are vital to the electrochemical performance [28–31].

Recently, superstructure unit Sb@Ni₆ ring constructed with six NiO₆ octahedral units connected to a central SbO₆ octahedron in the compound NaNi_{2/3}Sb_{1/3}O₂, which is similar to the Li@Mn₆ unit with six MnO₆ linked to a central LiO₆ in Li₂MnO₃, was demonstrated to facilitate high structural stability and good cycling reversibility along with promising energy capacity [32-34]. The imposed cationic ordering in the form of Ni_6 ring probably arises from the Ni-O-Ni 90° super-exchange interaction [34,35]. The high-symmetric Ni₆ ring guarantees a stable local oxygen environment with three Na, two Ni and one Sb neighbors, which is believed to effectively enhance the thermal stability, increase the redox potential and suppress the multiple phase transformations [32-34]. On such a basis, a systematic theoretical evaluation of this kind of superstructure unit and the role of the group-V element in the center will definitely be rewarding. An in-depth understanding on the structure-performance relationship could help pave the way for future design of honeycomb-ordered cathode materials.

E-mail addresses: lisn@pku.edu.cn (S. Li), panfeng@pkusz.edu.cn (F. Pan).

^{*} Corresponding authors.

Herein, we employ first principles calculations to evaluate $M@Ni_6$ super-structural units vs. the electrochemical properties of $ANi_{2/3}M_{1/3}O_2$ (A = Li and Na; M = As, Sb and Bi). We show that the smaller the size of M element, the stronger M–O bond and the higher structural stability would be expected. The voltage profile of the cathode and the evolution of oxidation states of Ni ions during charge/discharge are closely related to M element, while the overall disproportionation at composition $A_{1/3}Ni_{2/3}M_{1/3}O_2$ is universal for all compounds. By varying the degree of distortion of NiO $_6$ octahedron though size effect of M, the energy position of Ni-d bands can be actively modulated, which results in different electrochemical performance and allows for optimization of the cathodes. These findings could elucidate the nature of M@TM $_6$ superstructure units and provide a basic platform on which a honeycomb-ordered cathode with higher energy density and better cycling stability could be developed.

2. Computational methods

All the calculations were performed using the plane-wave based density functional theory (DFT) method as implemented in the Vienna ab initio simulation package (VASP) [36–39]. Projector augmented wave (PAW) potentials were used to probe valence-core interactions [40,41]. The Perdew–Burke–Ernzerhof (PBE) parametrization of the

generalized gradient approximation (GGA) was employed to describe the electron exchange and correlation [42]. In order to correctly characterize the localization of transition-metal d-electrons, the PBE+U method with a Hubbard-type potential to describe the d-part of the Hamiltonian was applied in all our calculations [43-45]. The value of 6.2 eV for the Hubbard U parameter of Ni ion was adopted from previous work [34]. The kinetic energy cutoff of 500 eV was employed in expanding the plane-wave basis set [34]. The k-point sampling density of at least 1000/(the number of atoms per cell) within the Monkhorst-Pack scheme was found to be sufficient for energy convergence [46]. The threshold for residual force was set to 0.01 eV/Å in structural optimization. Spin-polarization was considered in all our calculations. Only the ferromagnetic state was considered, since the energy difference between ferromagnetic and antiferromagnetic orders is approximately 1 meV per formula unit, substantially lower than that between different Li/Na-vacancy configurations (> 26 meV).

3. Results and discussion

Three kinds of phases are involved in the structural evolution of $ANi_{2/3}M_{1/3}O_2$ [33,34,47], i.e. O3, P3 and O1 (Fig. 1a–c), according to Delmas' notation [48]. The notions O and P denote octahedral and trigonal prismatic coordination of the Li/Na ions, respectively, and the

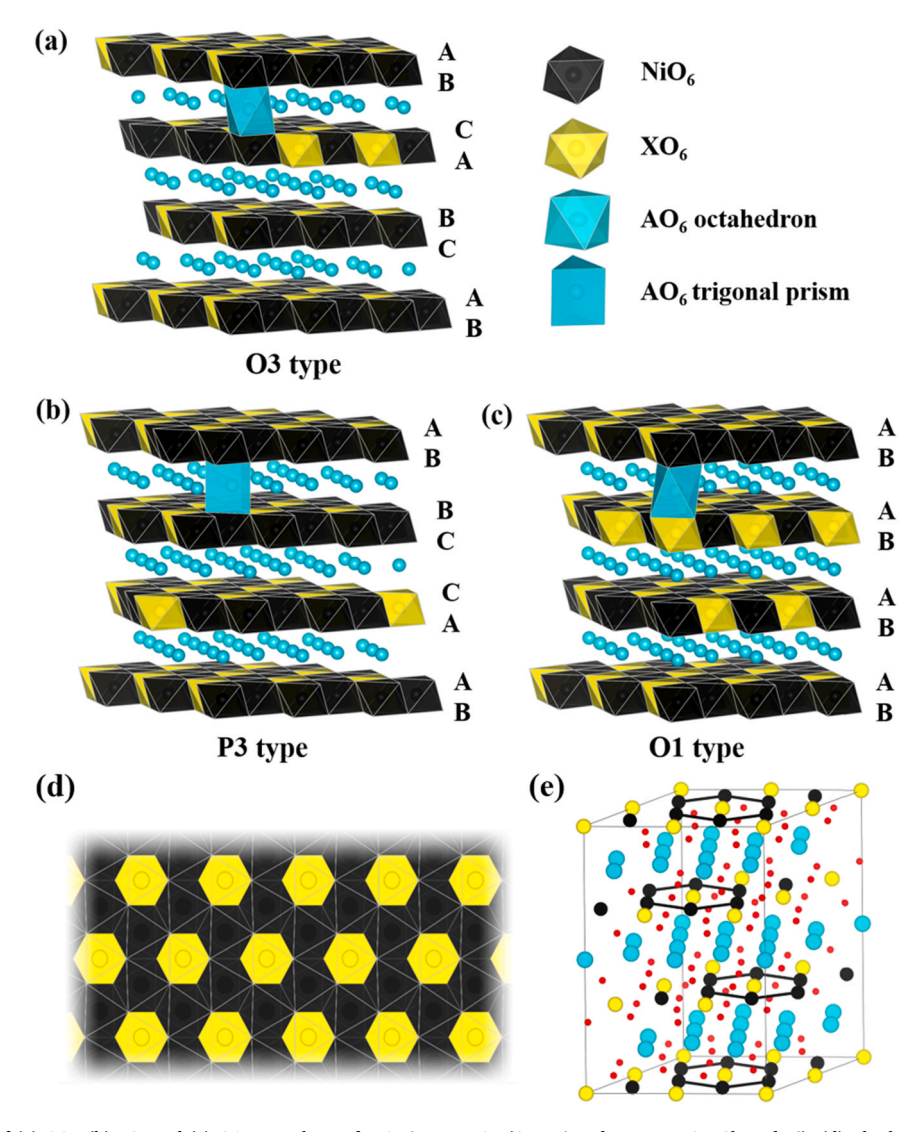


Fig. 1. Crystal structures of (a) O3-, (b) P3- and (c) O1-type phases for ANi_{2/3}M_{1/3}O₂ (A = Li and Na; M = As, Sb and Bi). (d) The honeycomb-like arrangement of NiO₆ and MO₆ octahedra. (e) Distribution of M@N₆ superstructure unit in O3-ANi_{2/3}M_{1/3}O₂.

indices 3 and 1 denote the minimum numbers of repeated transition metal layers [33,48]. Fig. 1d–e shows the honeycomb-like distribution of NiO₆ and MO₆ octahedra, all of which are edge-shared, identical to the way in LiCoO₂. For all the stoichiometric $ANi_{2/3}M_{1/3}O_2$ compounds, the most stable structure is O3-type, which is in agreement with experimental results [47].

First, we begin our analysis by establishing the relationship between the geometry of basic structure units in ANi_{2/3}M_{1/3}O₂ and the ionic radius of M. The ionic radii of As^{5+} , Sb^{5+} and Bi^{5+} are 0.46, 0.62 and 0.74 Å, respectively [49]. As shown in Fig. 2a, the size of NiO₆, MO₆ and AO₆ octahedra in O3-type ANi_{2/3}M_{1/3}O₂ increases monotonically with the increase in the radius of M. However, we notice that the volume increase of NiO6 and AO6 octahedra is much smaller than that of MO6 octahedron. Unlike AO6 octahedron which distributes in different layers from that of MO₆, the relatively small expansion of NiO₆ octahedron would mean that the size of M prefers to exert more influence on the degree of distortion of NiO6 octahedron rather than to directly alter the Ni–O bond length. We also find that the size of NiO₆ and AO₆ for ANiO₂, as provided in Fig. S1, is smaller than the corresponding value of the ANi_{2/3}M_{1/3}O₂ counterparts. This is due to a higher valence state of Ni ions in ANiO₂ (Ni³⁺) than in ANi_{2/3}M_{1/3}O₂ (Ni²⁺), which means a smaller ionic radius in the former case.

The degree of distortion of NiO₆ octahedron can be estimated from the O–Ni–O bond angle (Fig. 2b), in which the two O ions belong to different O layers (insets in Fig. 2b). There are two kinds of O–Ni–O bond angles, one related to the connection between two NiO₆ octahedra (θ_1) and the other related to the connection between NiO₆ and MO₆ octahedra (θ_2). Given that the Ni²⁺ ion exhibits an orbital occupation of $t_{2g}^6 e_g^2$, the ideal form of Ni²⁺O₆ should be a perfect octahedron, with identical Ni–O bond lengths and all O–Ni–O bond angles equal to 90°.

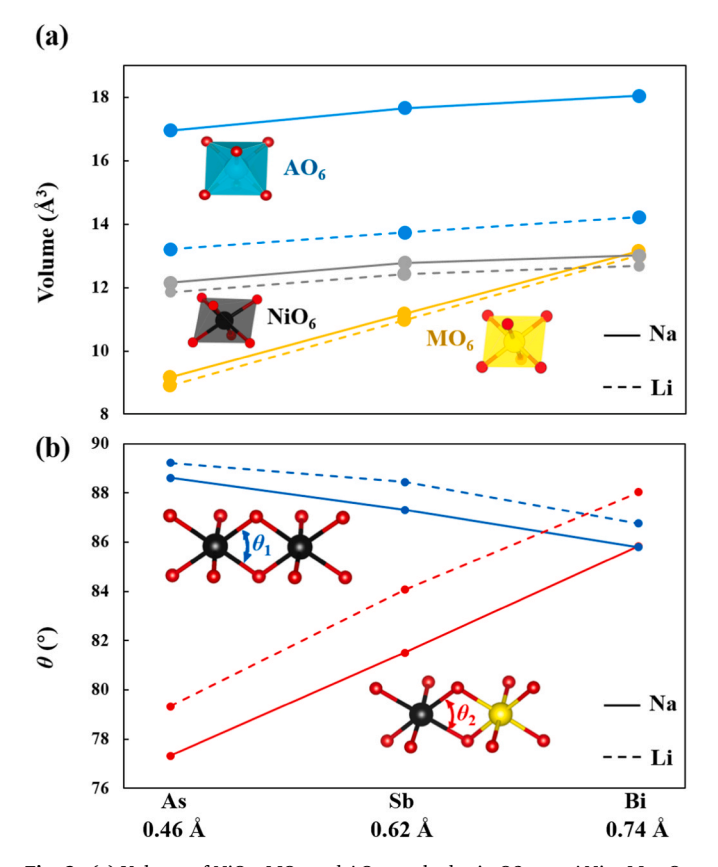


Fig. 2. (a) Volume of NiO₆, MO₆ and AO₆ octahedra in O3-type ANi_{2/3}M_{1/3}O₂. (b) O–Ni–O bond angle, θ . Two kinds of O–Ni–O bond angles are defined: θ_1 correlates with connection between two NiO₆ octahedra, and θ_2 correlates with connection between NiO₆ and MO₆ octahedra.

The ionic radius of Ni²⁺ is 0.69 Å, in between those of Sb⁵⁺ and Bi⁵⁺. It can be expected that when small size ions, i.e. As⁵⁺ and Sb⁵⁺, are located in the middle of the Ni₆ ring, the M@TM₆ superstructure unit would experience a tendency of contraction as compared to its natural form. Because the Ni-2O-Ni chain in the Ni₆ honeycomb framework is rather rigid, as substantiated by the value of close to 90° found for θ_1 , the NiO₆ octahedron would be distorted in such a way that the two O ions connecting Ni and M would approach one another, so that they can also be closer to the M ion. Therefore, we can see that the smaller the size of M, the lower the value of θ_2 is. On the other hand, when large size ion, Bi⁵⁺, is in the middle of the Ni₆ ring, the Ni-2O-Ni chain tends to be slightly stretched, resulting in a smaller θ_1 than those in $ANi_{2/3}As_{1/3}O_2$ and $ANi_{2/3}Sb_{1/3}O_2$, while the distortion of NiO_6 is relatively minor with θ_2 slightly below 90°. Following Tarascon et al., [50] we estimate the O-O distortion degree with the formula: $\Delta = \frac{1}{12} \sum_{i=1}^{12} \left[(d_i - \langle d \rangle) / \langle d \rangle \right]^2$, with d_i the individual O-O distance in NiO6 octahedron. It is found that the O-O distortion becomes higher with smaller radius of M (Fig. S2). The above results suggest that the size effect of M in M@TM6 superstructure unit can be generally characterized by the distortion of NiO₆ octahedron, which is in turn relevant to the electronic structure of $ANi_{2/3}M_{1/3}O_2$ and the electrochemical performance of the cathode. Moreover, we can see that all the θ_1 and θ_2 are smaller for Na compounds than their Li counterparts (Fig. 2b). Given that the ideal value of θ is 90° (without distortion), it can be inferred that the distortion of NiO6 is more severe for Na compounds. This is further substantiated by a larger value of Δ shown in Fig. S2. The above result is probably due to a less compact structure of Na compounds as indicated by the volumes of octahedra shown in Fig. 2a, which could allow for higher flexibility of O ions to accommodate the M ion.

In the following, we examine the phase transformation and the voltage curve during the process of alkali intercalation/deintercalation. Phase transition originates from the thermodynamic competition between different phases and can be investigated via the construction of convex hull [51]. O3-, P3- and O1-type structures are compared to find out the intermediate ground states at different deintercalation stages for $A_{1-x}Ni_{2/3}M_{1/3}O_2$. In order to reduce the computational burden of exhaustive enumeration in DFT calculations, the potential configurations are first evaluated by electrostatic energy through Ewald summation and only the low-energy configurations are taken into account for DFT calculations [52,53]. Thermodynamic stability is determined by the formation energy (E_f) of the configuration, which is calculated with respect to the initial end member O3-ANi_{2/3}M_{1/3}O₂ and the final end member (O3/P3/O1)-Ni_{2/3}M_{1/3}O₂ according to the following formula [54–57]:

$$E_{\rm f} = E \left[A_{1-x} N i_{2/3} M_{1/3} O_2 \right] - (1-x) E \left[A N i_{2/3} M_{1/3} O_2 \right] - x E \left[N i_{2/3} M_{1/3} O_2 \right]$$

where E is the DFT total energy of the unit in square brackets. The formation energies of different configurations and the corresponding convex hull are depicted in Fig. 3.

The predicted intermediate ground states in Fig. 3 indicate that all the compounds exhibit a phase transition from O3 to P3 during the alkali deintercalation process. For Na_{1-x}Ni_{2/3}As_{1/3}O₂, the O3 phase persists until x=1/3, while for other compounds, the two-phase transition tends to occur at the beginning of deintercalation. However, if we consider the lowest-energy configurations in 0 < x < 1/3 for Na_{1-x}Ni_{2/3}Sb_{1/3}O₂ and Na_{1-x}Ni_{2/3}Bi_{1/3}O₂, it is not so apparent that the two-phase transition will occur in this composition range, because the formation energies of O3-type intermediates are quite close to the convex hull. In this case, the energy for phase separation into a two-phase equilibrium of O3-ANi_{2/3}M_{1/3}O₂ and P3-A_{1-x}Ni_{2/3}M_{1/3}O₂ would be limited, which leaves room for a solid-solution pathway for deintercalation in O3 phase until x=1/3 [58]. On the contrary, Li compounds could only be stabilized in P3 phase for 0 < x < 2/3. The above result implies that at the beginning of deintercalation, Li_{1-x}Ni_{2/3}M_{1/3}O₂ cathodes are generally

Z. Hu et al. Nano Energy 83 (2021) 105834

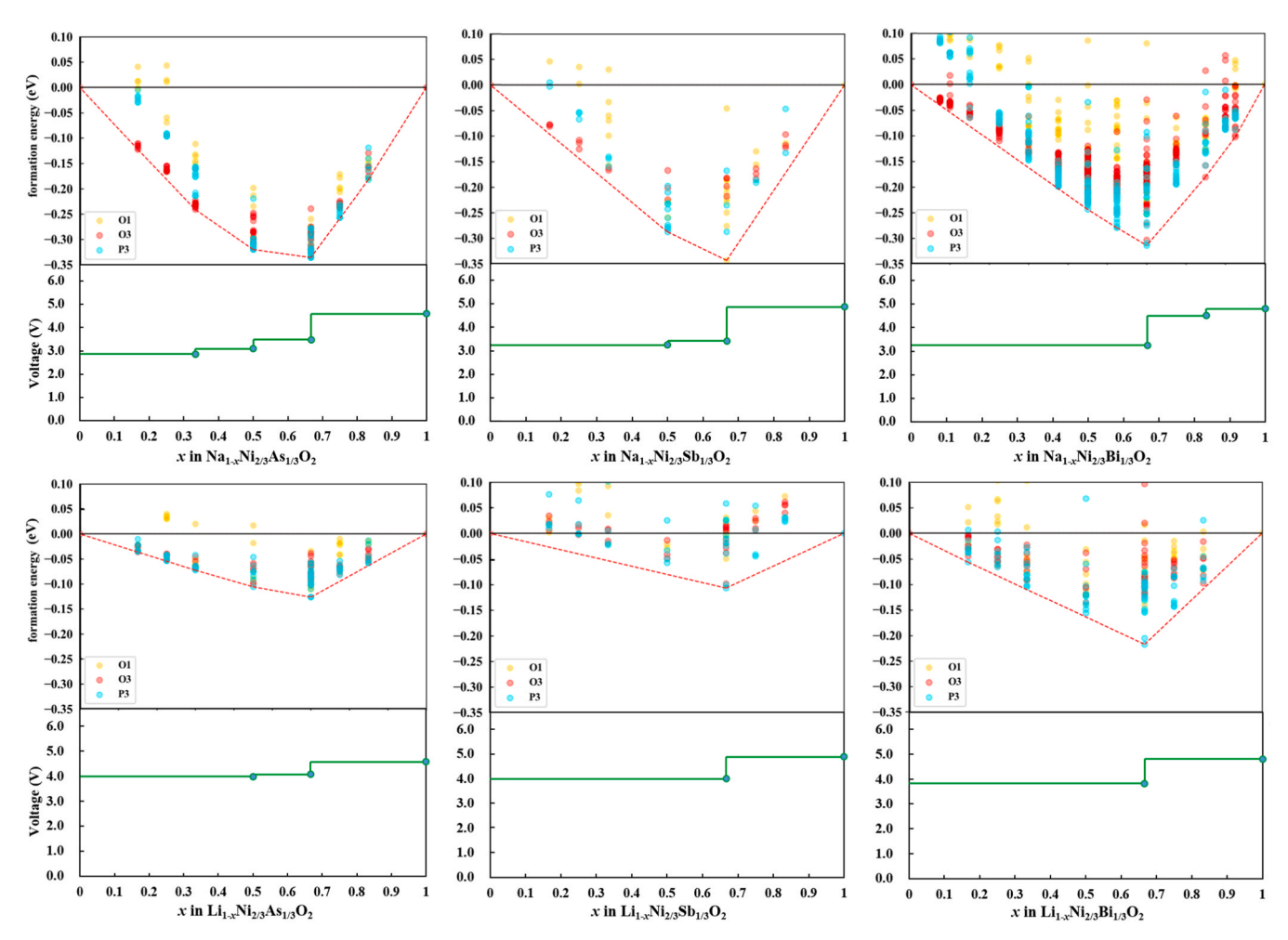
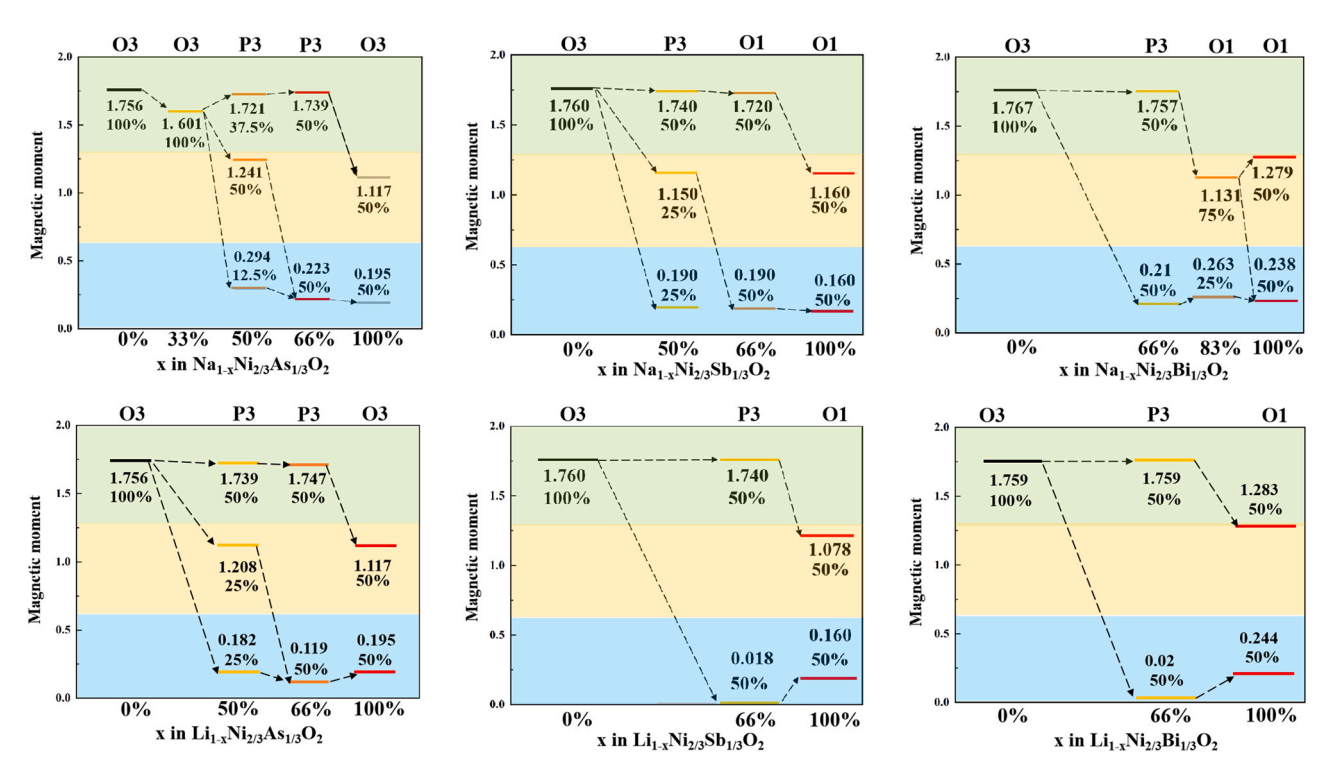


Fig. 3. The thermodynamic convex hull for $A_{1.x}N_{1/3}M_{1/3}O_2$ and the calculated average voltage curve at 0 K.



 $\textbf{Fig. 4.} \ \ \text{The magnetic moments of Ni ions in different intermediate phases for the } A_{1.x}Ni_{2/3}M_{1/3}O_2 \ cathodes.$

more susceptible to layer gliding than $Na_{1.x}Ni_{2/3}M_{1/3}O_2$ cathodes. Moreover, for $Na_{1.x}Ni_{2/3}As_{1/3}O_2$ and $Li_{1.x}Ni_{2/3}As_{1/3}O_2$, further deintercalation from P3 phase would lead to a phase transition back to O3 phase upon x>2/3, while for other compounds, the final end member $Ni_{2/3}M_{1/3}O_2$ is in O1 phase. This demonstrates the differential response of phase transition at low Li/Na limit to the variation in the size of M ion.

Based on the calculated formation energies of intermediate ground states, we can derive the voltage profile at 0 K via the following equation [59,60]:

indicating that they will not decompose spontaneously. In comparison to the oxygen vacancy formation energies in NaNiO₂ and LiNiO₂ (2.61 eV and 1.77 eV, respectively), the high $\Delta E_{V(O)}$ values in ANi_{2/3}M_{1/3}O₂ compounds demonstrate that the M element can effectively enhance the resistance to oxygen evolution. It is also found that smaller radius of M will lead to higher stability of the lattice oxygen atoms.

To better understand the underlying mechanism behind the high thermodynamic stability of $ANi_{2/3}M_{1/3}O_2$, we carry out the projected crystal orbital Hamilton population (COHP) [63–66] analysis to assess

$$\overline{V}(x_1, x_2) = -\frac{1}{(x_2 - x_1)e} \left\{ E\left[A_{x_2} Ni_{2/3} M_{1/3} O_2 \right] - E\left[A_{x_1} Ni_{2/3} M_{1/3} O_2 \right] - (x_2 - x_1) E[A] \right\}$$
(2)

where $\overline{V}(x_I,x_2)$ is the average voltage in the composition range of $x_I \le x \le x_2$ with respect to the alkali metal anode and E[A] is the total energy of a single Li/Na atom in its alkali-metal ground state. The calculated voltage for Na_{1-x}Ni_{2/3}Sb_{1/3}O₂ (3.2–3.5 eV) is consistent with previous experimental result [32–34]. For Li compounds, the voltage profiles indicate a trend that smaller size of M will be advantageous for higher voltage, while among the Na compounds, Na_{1-x}Ni_{2/3}Sb_{1/3}O₂ cathode shows the highest average voltage. Nevertheless, the difference in average voltages for all ANi_{2/3}M_{1/3}O₂ compounds is relatively small.

The valence state of Ni ions can be determined by the calculated magnetic moments, which are provided in Fig. 4. All the calculated magnetic moments of Ni ions in A_{1-x}Ni_{2/3}M_{1/3}O₂ fall into three classes: $0-0.3~\mu_B,~1.0-1.3~\mu_B$ and $1.6-1.8~\mu_B$. The corresponding Ni ions can be classified into Ni⁴⁺, Ni³⁺ and Ni²⁺, respectively [34,61,62]. Before deintercalation, all the Ni ions exist in divalent state, underpinning the claim that As, Sb and Bi ions are in 5+ state. We notice that for all the compounds at x = 2/3, half of the Ni ions are oxidized to Ni⁴⁺ and the other half remains in their original state. Given that the average valence state of Ni at A2/3Ni2/3M1/3O2 is 3+, an overall disproportionation of Ni³⁺ is evidenced, as described previously for Na_{2/3}Ni_{2/3}Sb_{1/3}O₂ [32–34]. This phenomenon could be due to the instability of Ni³⁺O₆ octahedron, which is severely distorted under Jahn-Teller effect. The MO₆ octahedron, in which the M-O bond lengths are nearly equal, might offer a high resistance to long-range cooperative Jahn-Teller distortion of the lattice and a strong tendency to high-symmetric structures. Moreover, we notice that the highly distorted Ni²⁺O₆ octahedra for $NaNi_{2/3}As_{1/3}O_2$, $NaNi_{2/3}Sb_{1/3}O_2$ and $LiNi_{2/3}As_{1/3}O_2$ (Fig. 2b) tend to aid in the stabilization of Ni³⁺O₆ octahedra at the composition A_{1/2}Ni_{2/3}M_{1/3}O₂. It is likely that the intrinsic distortion imposed by M and the strong M-O bonding can compensate the strain effects caused by local Jahn-Teller distortion, when the ratio of Ni³⁺ ions is small. Since the direct disproportionation of Ni^{3+} at each deintercalation step and the facile reordering of Ni²⁺/Ni⁴⁺ ions during the O3/P3 two-phase transition will presumably stimulate a high energy consumption, the stabilization of Ni³⁺ ions, which facilitates the gradual oxidation from Ni^{2+} to Ni^{3+} and then to Ni^{4+} , could potentially help reduce the polarization of the cathode. In this regard, A_{1-x}Ni_{2/3}M_{1/3}O₂ cathodes with larger size of M will be less favorable.

Thermodynamic stability against oxygen release is a key requirement for cathodes. To ascertain whether oxygen would release upon alkali deintercalation in $ANi_{2/3}M_{1/3}O_2$, we have calculated the oxygen vacancy formation energy according to the following formula:

$$\Delta E_{V(O)} = E[ANi_{2/3}M_{1/3}O_{6-x}] + x\mu_O - E[ANi_{2/3}M_{1/3}O_6]$$
(3)

where $\mu_{\rm O}$ is the reference chemical potential of oxygen (gas-phase ${\rm O}_2$ molecule) and x denotes the concentration of O vacancies per formula unit. As shown in Fig. 5a, all the compounds have positive $\Delta E_{\rm V(O)}$ values,

the bonding character between cations and oxygen. Following the conventional denotation of bonding (positive values) and antibonding (negative values) states, we provide -COHP for NaNi_{2/3}As_{1/3}O₂ in Fig. 5b. -COHP for other compounds are shown in Fig. S3 in the Supporting Information. States below 0 eV are occupied states, while those above are unoccupied states. It is shown that the M-O occupied states are mostly bonding, while the Ni-O occupied states near the Fermi level are antibonding, because they are the e_g orbitals. The integration of the COHP up to the Fermi level (ICOHP) is calculated (Fig. 5a), which can be employed to quantitatively estimate the bonding strength. We find that the ICOHP for M-O is substantially larger than that for Ni-O (Fig. S4), thus confirming the strong M-O covalent bonding. We also find that smaller size of M shows larger ICOHP for M-O. Given that M with smaller radius possesses a higher electronegativity, a more pronounced covalent character between M and O atoms would be expected from Bi to As, which can account for the trends in bonding strength and oxygen vacancy formation energy. Charge density difference was calculated to visualize the electron accumulation/depletion regions in LiNi_{2/3}M_{1/3}O₂ compounds, as shown in Fig. S5. The charge rehybridization between As and O is relatively more significant than the Sb-O and Bi-O counterparts, suggesting a stronger bonding of As-O bonds and consequently higher stability of LiNi_{2/3}As_{1/3}O₂ than other compounds [67,68].

Previous reports have demonstrated the anionic redox activity in Li@TM₆ superstructure units and revealed the importance of oxygen non-bonding states near the Fermi level for anionic redox [69–72]. Here we present in Figs. 6a and S6 the density of states (DOS) of ANi_{2/3}M_{1/3}O₂. An overlapping feature is observed between the O-p and Ni-d states near the Fermi level, reflecting the Ni-O bond covalency, while no oxygen non-bonding state is discernable. We have also examined the valence state of O during deintercalation and found there is little change (no larger than 0.2). Therefore, we can eliminate the possibility of oxygen ions acting as redox active centers for this kind of cathodes. Similar to other Ni-containing cathodes [73], both the Ni^{2+}/Ni^{3+} and Ni^{3+}/Ni^{4+} redox couples in $A_{1-x}Ni_{2/3}M_{1/3}O_2$ involve losing or adding an electron in the e_{g} orbitals. We investigate the variation in energy level of $e_{\rm g}$ orbitals for different M by using the upper bound of the occupied $e_{\rm g}$ bands as a rough estimate. The bottom of alkali-s bands is taken as the energy reference. From Fig. 6b we see that the upper band edge of e_g orbitals increases from As to Bi, and all the values for $ANi_{2/3}M_{1/3}O_2$ are lower than those for the $NaNiO_2$ and $LiNiO_2$ counterparts. This suggests that the energy level of $e_{\rm g}$ orbitals is affected by the presence of M and is a function of the size of M.

Now we try to establish the relationship between the distortion of NiO₆ octahedron and the electrochemical properties of $A_{1.x}Ni_{2/3}M_{1/3}O_2$ cathodes. As mentioned above, the two O ions linking NiO₆ and MO₆ octahedra tend to approach each other when the radius of M is smaller than Ni. Each NiO₆ is coordinated by three MO₆ octahedra (Fig. 6c), and therefore the distorted NiO₆ displays a D_{3d} symmetry, resembling that of IrO₆ octahedron in Li₂IrO₃ [74]. As the e_g orbitals point directly towards

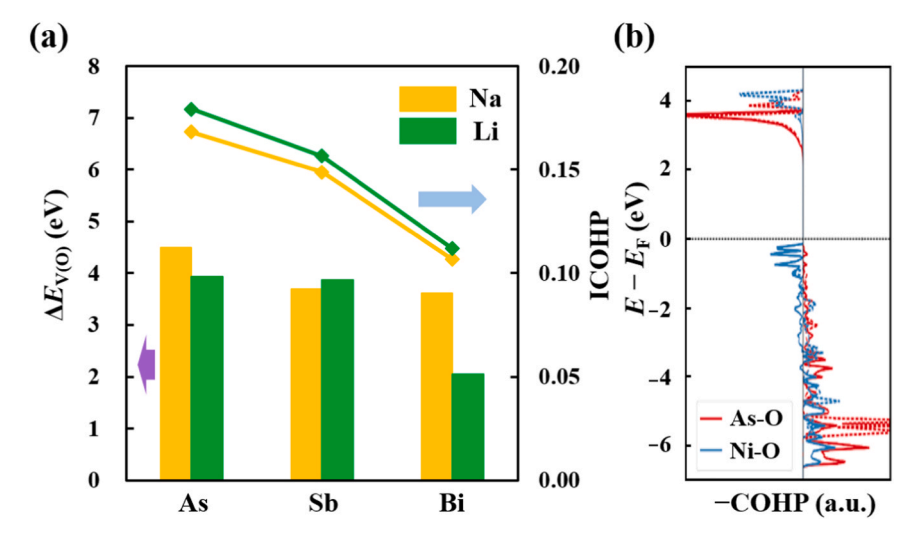


Fig. 5. (a) The oxygen vacancy formation energy, $\Delta E_{V(O)}$, and the integration of COHP up to the Fermi level, ICOHP, for M–O bonds. (b) Projected crystal orbital Hamilton population for Ni–O and As-O bonds in NaNi_{2/3}As_{1/3}O₂. Energies are referenced to the Fermi level (E_F).

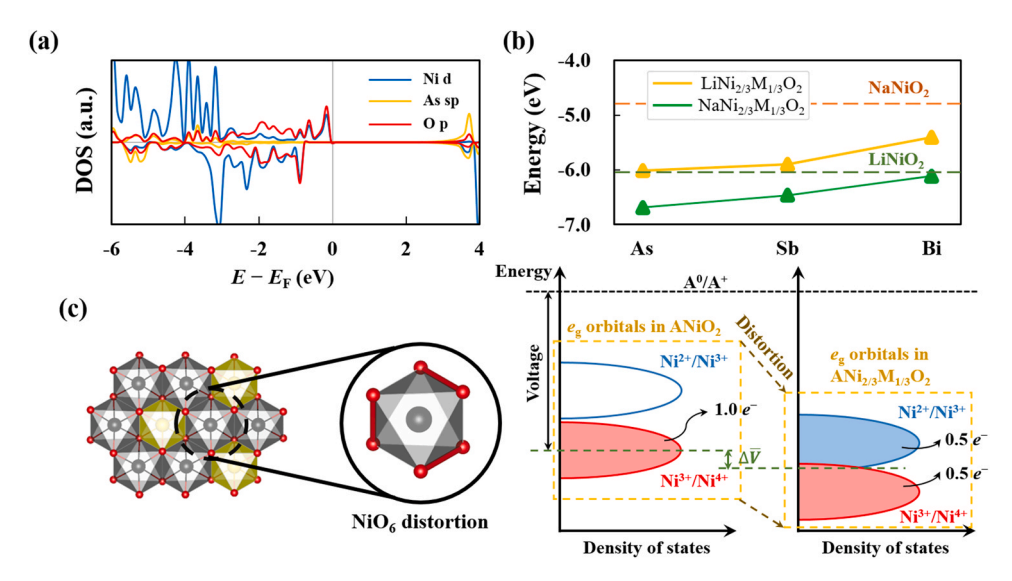


Fig. 6. (a) Localized DOS for NaNi_{2/3}As_{1/3}O₂. (b) The upper bound of the occupied e_g bands for ANi_{2/3}M_{1/3}O₂ as referenced to the bottom of alkali-s bands. (c) Schematic illustration of the distorted NiO₆ octahedron in M@Ni₆ superstructure unit, and the influence of distortion on the energy level of e_g bands.

the neighboring oxygen ligands in an ideal octahedral environment, such a distortion would reduce the overlap between Ni-d and O-p orbitals of $e_{\rm g}$ symmetry. Given that the $e_{\rm g}$ orbitals are antibonding, the energy level of e_g orbitals will decrease with increasing distortion, which can explain the trend shown in Fig. 6b. Although the distortion of NiO₆ in $ANi_{2/3}Bi_{1/3}O_2$ is relatively small, the elongation of Ni–O bonds could also contribute to a weaker d-p interaction and lower e_g bands. Consequently, the energy level of e_g orbitals will inevitably be lower in ANi_{2/3}M_{1/3}O₂ than in ANiO₂ counterparts. It is worth noting that the voltage of a Ni oxide cathode is closely related to the energy consumption for extracting an electron from the e_g bands. In ANi_{2/3}M_{1/3}O₂, half of the Ni²⁺ ions are to be oxidized to Ni⁴⁺ when the cathode is charged to $A_{1/3}Ni_{2/3}M_{1/3}O_2$, which involves the activation of both Ni^{2+}/Ni^{3+} and Ni³⁺/Ni⁴⁺ redox couples. In ANiO₂, only Ni³⁺/Ni⁴⁺ redox couple is activated. Therefore, the combined effect of lower band-energy induced by NiO₆ distortion and the propensity for disproportionation owing to the high-symmetric MO₆ octahedron, leads to the experimental observation that $NaNi_{2/3}Sb_{1/3}O_2$ cathode operates at higher voltage than NaNiO₂ [32-34]. In light of this, we can speculate that the voltage of $ANi_{2/3}M_{1/3}O_2$ cathodes may, to some extent, be modulated by the size of M. Smaller radius of M will be beneficial for higher voltage. Yet it should be noted that the AO $_6$ octahedron would also be destabilized by a highly distorted NiO $_6$ octahedron nearby (for example, in NaNi $_2/_3$ As $_1/_3$ O $_2$), which could reduce the energy cost of extracting the alkali ion and result in lower voltage. This may rationalize the voltage trend in NaNi $_2/_3$ M $_1/_3$ O $_2$ cathodes and the small difference in average voltage among different ANi $_2/_3$ M $_1/_3$ O $_2$ compounds.

4. Conclusion

Taking $ANi_{2/3}M_{1/3}O_2$ (A = Li and Na, and M = As, Sb and Bi) compounds as model systems, we have carried out a detailed first principles study of $M@Ni_6$ superstructure units in cathode materials to clarify the role of group-V elements on electrochemical properties. It is found that the M–O covalent bond strength decreases from As to Bi and higher thermodynamic stability can be expected with lower atomic number of M element. An overall disproportionation of Ni^{3+} ions will take place for all cathodes at the composition $A_{1/3}Ni_{2/3}M_{1/3}O_2$, which mediates the activation of both Ni^{2+}/Ni^{3+} and Ni^{3+}/Ni^{4+} redox couples. The distortion of NiO_6 octahedron is identified as a bridge between the

Z. Hu et al. Nano Energy 83 (2021) 105834

size of M and the electrochemical properties of $ANi_{2/3}M_{1/3}O_2$ cathodes including the average voltage and the polarization loss. Smaller size of M will contribute to more severe distortion of NiO_6 octahedron, which not only has a lower energy level of the $e_{\rm g}$ bands, but also facilitates the stabilization of Ni^{3+} ions. The former effect is in part responsible for higher voltage and the latter for lower polarization. In aggregate, these results can broaden our understanding of the $M@Ni_6$ superstructure units and provide the foundations for the design and development of honeycomb-ordered cathode materials.

CRediT authorship contribution statement

Zongxiang Hu: Data curation, Formal analysis, Investigation, Visualization, Writing - original draft. Mouyi Weng: Formal analysis, Writing - review & editing. Zhefeng Chen: Formal analysis. Wenchang Tan: Resources. Shunning Li: Conceptualization, Formal analysis, Investigation, Validation, Visualization, Writing - review & editing. Feng Pan: Conceptualization, Funding acquisition, Project administration, Resources, Supervision, Writing - review & editing.

Declaration of Competing Interest

The authors declare that they have no known competing financial interests or personal relationships that could have appeared to influence the work reported in this paper.

Acknowledgements

This work was financially supported by National Key R&D Program of China (2016YFB0700600), Soft Science Research Project of Guangdong Province (No. 2017B030301013), and Shenzhen Science and Technology Research Grant (ZDSYS201707281026184).

Appendix A. Supporting information

Supplementary data associated with this article can be found in the online version at doi:10.1016/j.nanoen.2021.105834.

References

- [1] D. Wang, C. Xin, M. Zhang, J. Bai, J. Zheng, R. Kou, J.Y. Peter Ko, A. Huq, G. Zhong, C.-J. Sun, Y. Yang, Z. Chen, Y. Xiao, K. Amine, F. Pan, F. Wang, Chem. Mater. 31 (2019) 2731–2740.
- [2] N. Yabuuchi, K. Kubota, M. Dahbi, S. Komaba, Chem. Rev. 114 (2014) 11636–11682.
- [3] J. Hu, J. Zhang, Chin. J. Struct. Chem. 38 (2019).
- [4] L. Tong-Chao, P. Feng, K. Amine, Chin. J. Struct. Chem. 39 (2020) 11–15.
- [5] J. Lu, Z. Chen, Z. Ma, F. Pan, L.A. Curtiss, K. Amine, Nat. Nanotechnol. 11 (2016), 1031.
- [6] Z. Ze, W. Mou-Yi, Y. Lu-Yi, H. Zong-Xiang, C. Zhe-Feng, P. Feng, Chin. J. Struct. Chem. 38 (2019) 2020–2026.
- [7] A. Kelly, K.M. Knowles, Crystallography and Crystal Defects, John Wiley & Sons, USA, 2012.
- [8] J. Miao, P. Ercius, S.J. Billinge, Science 353 (2016).
- [9] R.A. House, U. Maitra, M.A. Perez-Osorio, J.G. Lozano, L. Jin, J.W. Somerville, L.C. Duda, A. Nag, A. Walters, K.J. Zhou, M.R. Roberts, P.G. Bruce, Nature, doi:10.10 38/s41586-019-1854-32019.
- [10] Y. Qi, Q. Xu, A. Van der Ven, J. Electrochem. Soc. 159 (2012) A1838-A1843.
- [11] W.H. Woodford, Y.-M. Chiang, W.C. Carter, J. Electrochem. Soc. 160 (2013) A1286–A1292.
- [12] A.J. Toumar, S.P. Ong, W.D. Richards, S. Dacek, G. Ceder, Phys. Rev. Appl. 4 (2015), 064002.
- [13] C. Didier, M. Guignard, M.R. Suchomel, D. Carlier, J. Darriet, C. Delmas, Chem. Mater. 28 (2016) 1462–1471.
- [14] J. Vinckevičiu te, M.D. Radin, A. Van der Ven, Chem. Mater, 28, 2016, pp. 8640–8650.
- [15] Y. Xiao, Y.F. Zhu, H.R. Yao, P.F. Wang, X.D. Zhang, H. Li, X. Yang, L. Gu, Y.C. Li, T. Wang, Y.X. Yin, X.D. Guo, B.H. Zhong, Y.G. Guo, Adv. Energy Mater. 9 (2019), 1803978
- [16] S.P. Ong, V.L. Chevrier, G. Hautier, A. Jain, C. Moore, S. Kim, X. Ma, G. Ceder, Energ. Environ. Sci. 4 (2011) 3680–3688.
- [17] X. Ma, H. Chen, G. Ceder, J. Electrochem. Soc. 158 (2011), A1307.
- [18] L. Wang, B. Chen, J. Ma, G. Cui, L. Chen, Chem. Soc. Rev. 47 (2018) 6505–6602.

- [19] D. Chang, H. Huo, K.E. Johnston, M. Ménétrier, L. Monconduit, C.P. Grey, A. Van der Ven, J. Mater. Chem. A 3 (2015) 18928–18943.
- [20] C. Luo, A. Langrock, X. Fan, Y. Liang, C. Wang, J. Mater. Chem. A 5 (2017) 18214–18220.
- [21] E. Talaie, S.Y. Kim, N. Chen, L.F. Nazar, Chem. Mater. 29 (2017) 6684-6697.
- [22] P.F. Wang, H.R. Yao, X.Y. Liu, Y.X. Yin, J.N. Zhang, Y. Wen, X. Yu, L. Gu, Y.G. Guo, Sci. Adv. 4 (2018), eaar6018.
- [23] L. Wang, Y.-G. Sun, L.-L. Hu, J.-Y. Piao, J. Guo, A. Manthiram, J. Ma, A.-M. Cao, J. Mater. Chem. A 5 (2017) 8752–8761.
- [24] M.-J. ZHANG, Y.-S. CHEN, F. PAN, Y. REN, Chin. J. Struct. Chem. (2020), 6.
- 25] G. Singh, N. Tapia-Ruiz, J.M. Lopez Del Amo, U. Maitra, J.W. Somerville, A. R. Armstrong, J. Martinez de Ilarduya, T. Rojo, P.G. Bruce, Chem. Mater. 28 (2016) 5087-5004
- [26] P.F. Wang, Y. You, Y.X. Yin, Y.S. Wang, L.J. Wan, L. Gu, Y.G. Guo, Angew. Chem. Int. Ed. 55 (2016) 7445–7449.
- [27] W. Zhao, H. Kirie, A. Tanaka, M. Unno, S. Yamamoto, H. Noguchi, Mater. Lett. 135 (2014) 131–134.
- [28] J. Zheng, Y. Ye, F. Pan, Natl. Sci. Rev. 7 (2020) 242-245.
- [29] Y. Li, L. Xie, Z. Zheng, Z.-W. Yin, J. Li, M. Weng, J. Liu, J. Hu, K. Yang, G. Qian, B. Cao, Z. Li, S. Xu, W. Zhao, S. Li, J. Sun, M. Zhang, F. Pan, Nano Energy 77 (2020), 105157.
- [30] C.Y. Chen, J. Rizell, G.M. Kanyolo, T. Masese, Y. Sassa, M. Mansson, K. Kubota, K. Matsumoto, R. Hagiwara, Q. Xu, Chem. Commun. (Camb.) 56 (2020) 9272–9275.
- [31] L. Xiao, Z. Ding, C. Chen, Z. Han, P. Wang, Q. Huang, P. Gao, W. Wei, iScience 23 (2020), 100898.
- [32] D. Yuan, X. Liang, L. Wu, Y. Cao, X. Ai, J. Feng, H. Yang, Adv. Mater. 26 (2014) 6301–6306.
- [33] P.-F. Wang, H.-R. Yao, Y. You, Y.-G. Sun, Y.-X. Yin, Y.-G. Guo, Nano Res 11 (2018) 3258–3271.
- [34] P.F. Wang, M. Weng, Y. Xiao, Z. Hu, Q. Li, M. Li, Y.D. Wang, X. Chen, X. Yang, Y. Wen, Y.X. Yin, X. Yu, Y. Xiao, J. Zheng, L.J. Wan, F. Pan, Y.G. Guo, Adv. Mater. 31 (2019), e1903483.
- [35] Z. Hu, J. Zheng, C. Xin, G. Teng, Y. Zuo, F. Pan, J. Phys. Chem. C. 122 (2018) 4125–4132.
- [36] G. Kresse, J. Hafner, Phys. Rev. B 47 (1993), 558.
- [37] G. Kresse, J. Furthmüller, Phys. Rev. B 54 (1996), 11169.
- [38] S. Mishra, G. Ceder, Phys. Rev. B 59 (1999) 6120.
- [39] G. Kresse, J. Furthmüller, Comp. Mater. Sci. 6 (1996) 15-50.
- [40] P.E. Blöchl, Phys. Rev. B 50 (1994), 17953.
- [41] G. Kresse, D. Joubert, Phys. Rev. B 59 (1999), 1758.
- [42] J.P. Perdew, K. Burke, M. Ernzerhof, Phys. Rev. Lett. 77 (1996), 3865.
- [43] S. Dudarev, G. Botton, S. Savrasov, C. Humphreys, A. Sutton, Phys. Rev. B 57 (1998), 1505.
- [44] V.I. Anisimov, J. Zaanen, O.K. Andersen, Phys. Rev. B 44 (1991), 943.
- [45] V.I. Anisimov, I. Solovyev, M. Korotin, M. Czyżyk, G. Sawatzky, Phys. Rev. B 48 (1993), 16929.
- [46] H.J. Monkhorst, J.D. Pack, Phys. Rev. B 13 (1976), 5188.
- [47] P.-F. Wang, Y.-J. Guo, H. Duan, T.-T. Zuo, E. Hu, K. Attenkofer, H. Li, X.S. Zhao, Y.-X. Yin, X. Yu, Y.-G. Guo, ACS Energy Lett. 2 (2017) 2715–2722.
- [48] C. Delmas, C. Fouassier, P. Hagenmuller, Phys. B+ C. 99 (1980) 81-85.
- [49] R.T. Shannon, C.T. Prewitt, Acta Crystallogr. Sect. B: Struct. Crystallogr. Cryst. Chem. 25 (1969) 925–946.
- [50] P.E. Pearce, A.J. Perez, G. Rousse, M. Saubanere, D. Batuk, D. Foix, E. McCalla, A. M. Abakumov, G. Van Tendeloo, M.L. Doublet, J.M. Tarascon, Nat. Mater. 16 (2017) 580–586
- [51] D.A. Kitchaev, S.T. Dacek, W. Sun, G. Ceder, J. Am. Chem. Soc. 139 (2017) 2672–2681.
- [52] P.P. Ewald, Ann. der Phys. 369 (1921) 253–287.
- [53] T. Chen, G. Sai Gautam, W. Huang, G. Ceder, Chem. Mater. 30 (2018) 153-162.
- [54] A. Van der Ven, M. Aydinol, G. Ceder, G. Kresse, J. Hafner, Phys. Rev. B 58 (1998), 2975.
- [55] M. Wagemaker, A. Van Der Ven, D. Morgan, G. Ceder, F. Mulder, G. Kearley, Chem. Phys. 317 (2005) 130–136.
- [56] S. Li, J.-B. Liu, Q. Wan, J. Xu, B.-X. Liu, Chem. Mater. 29 (2017) 10075–10087.
- [57] A. Vasileiadis, B. Carlsen, N.J.J. de Klerk, M. Wagemaker, Chem. Mater. 30 (2018) 6646–6659.
- [58] R. Malik, F. Zhou, G. Ceder, Nat. Mater. 10 (2011), 587.
- [59] M. Aydinol, A. Kohan, G. Ceder, K. Cho, J. Joannopoulos, Phys. Rev. B 56 (1997), 1354
- [60] M.S. Islam, C.A. Fisher, Chem. Soc. Rev. 43 (2014) 185–204.
- [61] B. Hwang, Y. Tsai, D. Carlier, G. Ceder, Chem. Mater. 15 (2003) 3676-3682.
- [62] H. Yu, Y. Qian, M. Otani, D. Tang, S. Guo, Y. Zhu, H. Zhou, Energ. Environ. Sci. 7 (2014) 1068–1078.
- [63] R. Dronskowski, P.E. Blöchl, J. Phys. Chem. 97 (1993) 8617–8624.
- [64] V.L. Deringer, A.L. Tchougréeff, R. Dronskowski, J. Phys. Chen. A 115 (2011) 5461–5466.
- [65] S. Maintz, V.L. Deringer, A.L. Tchougréeff, R. Dronskowski, J. Comput. Chem. 34 (2013) 2557–2567.
- [66] S. Maintz, V.L. Deringer, A.L. Tchougréeff, R. Dronskowski, J. Comput. Chem. 37 (2016) 1030–1035.
- [67] L. Xiao, Z. Ding, Q. Huang, C. Chen, Y. Feng, C. Liang, P. Gao, W. Wei, Acta Mater. 199 (2020) 34–41.
- [68] M. Ihsan-Ul-Haq, H. Huang, J. Wu, J. Cui, S. Yao, W.G. Chong, B. Huang, J.-K. Kim, Nano Energy 71 (2020), 104613.

- [69] M. Saubanère, E. McCalla, J.-M. Tarascon, M.-L. Doublet, Energ. Environ. Sci. 9 (2016) 984–991.
- [70] Y. Xie, M. Saubanère, M.-L. Doublet, Energ. Environ. Sci. 10 (2017) 266–274.
- [71] D.-H. Seo, J. Lee, A. Urban, R. Malik, S. Kang, G. Ceder, Nat. Chem. 8 (2016), 692.
- [72] G. Assat, J.-M. Tarascon, Nat. Energy 3 (2018) 373–386.
- [73] E. Hu, X. Yu, R. Lin, X. Bi, J. Lu, S. Bak, K.-W. Nam, H.L. Xin, C. Jaye, D.A. Fischer, Nat. Energy 3 (2018) 690–698.
- [74] P.E. Pearce, A.J. Perez, G. Rousse, M. Saubanère, D. Batuk, D. Foix, E. McCalla, A. M. Abakumov, G. Van Tendeloo, M.-L. Doublet, Nat. Mater. 16 (2017) 580–586.



Zongxiang Hu received his Ph.D. degree under the supervision of Prof. Feng Pan at School of Advanced Materials, Peking University Shenzhen Graduate School. His current research mainly focuses on the application of first principles calculation to investigate the thermodynamics and electrochemical properties of layered transition metal oxide cathode materials.



Mouyi Weng received his Ph.D. degree from Peking University Shenzhen Graduate School, China. He received his B.S. degree from Tsinghua University in 2015. His research interests include: computational materials, materials simulation algorithms and electronic structure calculation in materials.



Zhefeng Chen received his B.E. degree in 2018 from School of Physics, Peking University, China. He is now a postgraduate student in the School of Advanced Materials, Peking University, Shenzhen Graduate School, China. His research interests include first-principles design of energy storage materials.



Wenchang Tan received his Ph.D. degree in 1997 from Shandong University, China. Now he is professor and doctoral supervisor of The Department of Mechanics and Aerospace Technology, School of Engineering, Peking University. He has long been engaged in the research work of biomechanics and non-Newtonian fluid mechanics, including intracellular calcium signal conduction, biomechanics of calcium spark, hemodynamics, mechanical analysis and numerical simulation of cardiovascular diseases, quantitative physiology, fractional anomalous diffusion, viscoelastic fluid mechanics, heat flow and micro-flow in porous media, etc.



Shunning Li received his B.E. degree in 2013 and Ph.D. degree in 2018 from School of Materials Science and Engineering, Tsinghua University, China. Currently, he is an assistant research fellow at the School of Advanced Materials, Peking University, Shenzhen Graduate School, China. His research interest focuses on the first-principles design of energy storage materials and heterogeneous catalysts.



Feng Pan got his B.S. degree from Department of Chemistry, Peking University in 1985 and Ph.D. degree from Department of P&A Chemistry, University of Strathclyde, UK, with "Patrick D. Ritchie Prize" for the best Ph.D. in 1994. Now he is a National 1000-plan Professor, Founding Dean of School of Advanced Materials, Peking University Shenzhen Graduate School, and Director of National Center of Electric Vehicle Power Battery and Materials for International Research. He is engaged in fundamental research and product development of novel energy conversion and storage materials & devices.